Explosion driven Interfacial instabilities of granular media

Kun Xue[a*], Xiaoliang Shi[a], Junsheng Zeng[b], Baolin Tian[c], Panpan Han[a], Jiarui Li[a], Lan Liu[a], Baoqing Meng[c] , Xiaohu Guo[d], Chunhua Bai[a],

[a] State Key Laboratory of Explosive Science and Technology, Beijing Institute of Technology, Beijing, 100081;[b] College of Engineering, Peking University, Beijing, 100094; [c]Institute of Applied Physics and Computational Mathematics, Beijing, 1000871; [d]Daresbury Laboratory, UK

Abstract

In this work, we investigate the evolution of a Richtmyer-Meshkov (RM)-like instability occurring on the internal surface of particle rings impinged by divergent blast waves. Despite of the signature spike-bubble instability structure analogous to the hydrodynamic RM instability, the growth of the perturbation amplitude in granular media undergoes an exponential phase followed by a linear phase, markedly differing from the hydrodynamic RM instability, indicating a fundamentally different mechanism. The granular RM-like instability arises from the incipient transverse granular flows induced by the hydrodynamic effects upon the shock interaction. Whereas a substantial perturbation growth is initiated by the ensuing rarefaction dilation when the hydrodynamic effects are minimum. It is the interplay between the localized transverse and radial granular flows that sustains the persistent perturbation growth and drives the morphological changes of instability pattern alongside.

Introduction

So-called jetting or fingering instabilities of dense granular media arise from the destabilized granular surfaces impinged by shock/blast waves, which have fundamental bearing on a range of natural phenomena and engineering processes, significantly for explosions of supernovas, volcanic eruptions, and laser-driven inertial confinement fusion experiments, etc[1]. The shocked gases thrust into the granular medium with the particle fingers protruding into the gases, forming a spike-like pattern[2-5], which bears a resemblance to a classic hydrodynamic instability known as Richtmyer-Meshkov (RM) instability occurring on shock swept corrugated interfaces between two materials of different densities or compressibilities[6-9]. Since granular materials are often modeled as viscoplastic fluids whereby a variety of dense granular flow profiles has been successfully described and predicted[10-14], it is tempted to assume the shock driven interfacial instability of granular media is the counterpart of the RM instability. Actually another important interfacial instability, the viscous fingering of granular media invaded by fluids is regarded as the granular equivalent of the Saffman-Taylor instability in the zero-surface-tension limit of normal fluid fingering, although the friction-induced dissipation yields the distinct scaling law for the finger width[15-17]. An exception can be found in the gravity driven granular analog of the Rayleigh-Taylor (RT) instability, which albeit mimicking those observed

in conventional fluids, has different underlying mechanisms thanks to the coupling of dry granular dynamics and the hydrodynamics of the interstitial fluid[18, 19].

The granular medium is fundamentally a multi-phase system with intrinsic discreteness. The interaction between constituent grains gives rise to the heterogeneous force transmission and localized granular flows[5, 20-22]. The interaction between grain skeleton and gas flows through pores, also prevalent in the granular RT-like instability, render a compaction wave through contact points between grains and an induced gas flow in the wake of a transmitted wave in the shocked granular media[23, 24]. Hence the non-Newtonian fluid approximation would smooth out the inter-phase physics and the discreteness underpinning the macroscopic behavior of shocked granular media and the resultant instabilities. Accordingly applying any variant of RM theory based on the continuum mechanics to the shock induced granular instability should be questionable. Specifically, besides the pressure impulse which is the dominant driving force in the RM instability, the particle collision, drag forces, and diffusion pressure gradient should be taken into account, although their relative importance is unclear. Furthermore, granular materials can be significantly compacted when exposed to explosion and subsequently undergo considerable dilation in the wake of the reflected rarefaction wave from the end boundary, even crossover to the dilute granular flows[25-28]. The density of granular media hence markedly changes throughout the growth of instabilities. Whereas in the hydrodynamic RM instability, the compressibility is mainly taken into account during the linear growth phase[29]. Thereafter the flows are

regarded as incompressible in most models, failing to account for the persistent dilation. Therefore, the hydrodynamic RM instability theories are intrinsically inadequate to describe the shock driven interfacial instability of granular media. In this work, we aim to quantitatively characterize the growth regimes of granular RM-like instabilities which are to be compared with the classic RM instability prediction. Alongside the Particle Image Velocimetry (PIV) technology which provides us limited access to the deformation of the skeleton materials[30, 31], a grain-scale numerical method, namely coarse-grained compressible computational fluid dynamics-discrete parcel method (CCFD-DPM)[14, 32, 33], enables us properly account for the roles played by various forces alluded above. A physical understanding of granular RM-like instabilities is put forth to shed light on the initiation and different growth regimes of instabilities.

Experimental setup

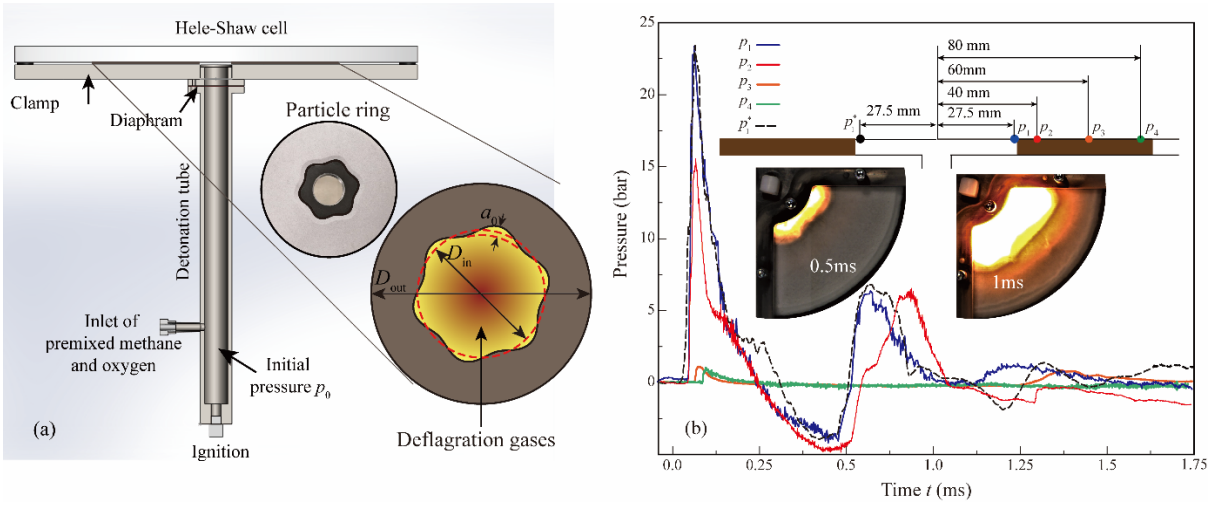

Figure 1. (a) Schematic of the experiment setup consisting of a vertical detonation tube (length: 400 mm; inner diameter: 30mm) and a radial Hele-Shaw cell (diameter: 500 mm). Inset: image of a

prepared particle ring (above) and schematic of the particle ring with an imposed internal surface (below). (b) Pressure histories at the internal surface of ring (p_1 and p_1^*) and inside the ring (p_2, p_3 and p_4) at p_0 = 1 bar. The coincidence between $p_1(t)$ and $p_1^*(t)$ which register the pressures at locations with the same radii but different azimuthal angles indicates the homogeneity of the shock loading. The propagation velocity of the transmitted wave can be calculated from the arrival time differences of pressure impulses at different locations, V_{tr} ~ 1000 m/s. Insets: the snapshots of shock dispersed particle rings at 0.5 (left) and 1.0 ms(right). Note that the capture of images is synchronized with the pressure recording.

Our experiment setup (see Fig. 1(a)) consists of a radial Hele-Shaw cell whose bottom plate with a central orifice is connected with a vertical detonation tube (volume ~272 ml) filled with the stoichiometric methane-oxygen premixed gases with varied initial pressure p_0. A freestanding densely packed thin particle ring (packing density ρ_p ~ 0.6) consisting of glass spheres (Fuji Manufacturing Japan) with a height of 5 beads was confined in between the bottom and top plates of the cell. A single-mode perturbation in cylindrical geometry was imposed on the internal surface of ring (see the inset in Fig. 1(a)), which can be parametrized as $r(\theta) = R_{in,0} + a_0 \cos(n\theta)$, where $R_{in,0}$ refers to the mean radius of the initial interface, a_0 to the initial amplitude, θ to the azimuthal angle and n to the azimuthal mode number, here n = 6. The deflagration inside the detonation tube issues a divergent cylindrical blast wave into the Hele-Shaw cell followed by the ever-expanding product gases. The pressure impulses recorded at the vicinities of the internal surface of ring (see Fig.1 (b)) feature a prominent first peak and a much reduced second peak during the first millisecond. The much subdued second peak results from the shock reflected from

the close end of the detonation tube. The transmitted compressive wave inside the ring decays rapidly with the overpressure only a fraction of the incident shock as seen in Fig.1(b), indicating an attenuated gas-particle coupling effect in the bulk of ring which is also corroborated by our simulation results. Note that the external surface of ring remains stationary (see insets of Fig. 1(b)) well after the propagation of transmitted disturbances. Varying the initial pressure of the premixed gases, p_0, from 0.7 to 1.5 bar can increase the peak overpressure of incident shocks from 10 to 30 bar, with Mach number varying from 4.6 to 5.9. The hydrodynamics inside the detonation tube and the Hele-shaw cell was accessed by simulations as elaborated in *Appendix I*. The pressure histories inside the cell induced by the deflagration of premixed gases with different initial pressures are presented in *Appendix II*.

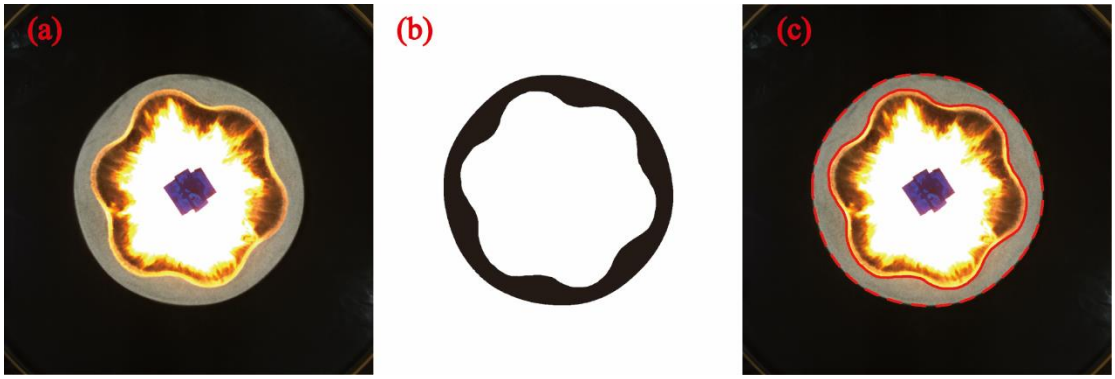

Figure 2 (a)preprocessed high-speed image of the shock dispersed particle ring. (b) Binarized image of (a) where the particle ring and gases are colored black and white, respectively. (c) Superimposition of the extracted boundaries of particle ring from (b) onto (a).

The optical images were obtained using a high-speed camera (Photron Fastcam SA 5) and processed by Image Pro Plus and MATLAB. Through the light intensity threshold, the preprocessed images (see Fig. 2(a)) were binarized as shown in Fig.

2(b) in which the particle ring is black in contrast with the white background gases. Then boundaries in the binary images were attained by the Sobel operator which are superposed onto the original images (See Fig. 2(c)) to check whether the boundary extraction is correct.

In order to calculate the velocity fields inside the particle ring using Particles image velocimetry(PIV), 10% of particles (by volume) were blacken to introduce the markers into the particle ring. The frame-to-frame velocity fields were obtained with PIVlab, a MATLAB based digital image correlation software[34]. The basic principle of PIVlab is to cross-correlate subwindows (interrogation window) of one image with an image taken at a later time, and then calculate the Eulerian velocity vectors of the assemble of particles in the subwindows. Before calculating the velocity fields of particles, the images first undergo pre-processing, the image contrast being enhanced using the algorithm called Contrast Limited Adaptive Histogram Equalization (CLAHE, window size=8 pixels). Different size of the PIV interrogation window (40×40, 24×24 and 20×20 pixels) was adopted for different experiments to optimize the calculated velocity fields. Once the velocities were determined, a Stdev filter(n=7) and local mean filter were applied to detect outliers.

Numerical method

The numerical simulations were conducted based on the coarse grained Compressible Computational Fluid Mechanics – Discrete Parcel Method (CCFD-DPM) method[14]. For the gas phase, the volume-averaged governing equations (Eqs.

1-3) constructed in the Eulerian frame are based on a transport five-equation model, i.e. a simplified form of Baer-Nunziato (B-N) model [35].

$$\frac{\partial\left(\alpha_f \left\langle \rho_f \right\rangle\right)}{\partial t} + \nabla \cdot \left(\alpha_f \left\langle \rho_f \right\rangle \tilde{\vec{u}}_f\right) = 0, \tag{1}$$

$$\begin{aligned} &\frac{\partial\left(\alpha_f \left\langle \rho_f \right\rangle\right)}{\partial t} + \nabla \cdot \left(\alpha_f \left\langle \rho_f \right\rangle \tilde{\vec{u}}_f \tilde{\vec{u}}_f + \alpha_f \left\langle p_f \right\rangle\right) \\ &\qquad = \left\langle p_f \right\rangle \nabla \alpha_f + \sum_i \left\{\alpha_{p,i} \rho_{p,i} D_{p,i} \left(\vec{u}_{p,i} - \left(\tilde{\vec{u}}_f\right)_i\right)\right\} \end{aligned}, \tag{2}$$

$$\begin{aligned} &\frac{\partial\left(\alpha_f \left\langle \rho_f \right\rangle \tilde{E}_f\right)}{\partial t} + \nabla \cdot \left(\alpha_f \left\langle \rho_f \right\rangle \tilde{E}_f \tilde{\vec{u}}_f + \alpha_f \left\langle p_f \right\rangle \tilde{\vec{u}}_f\right) \\ &\qquad = \left\langle P_f \right\rangle \nabla \alpha_f \cdot \tilde{\vec{u}}_p + \sum_i \left\{\alpha_{p,i} \rho_{p,i} D_{p,i} \left(\vec{u}_{p,i} - \left(\tilde{\vec{u}}_f\right)_i\right) \cdot \vec{u}_{p,i}\right\} \end{aligned}, \tag{3}$$

where α_f is the fluid volume fraction, ρ_f is the fluid density, $\vec{u}_f$ is the fluid velocity, p_f is the fluid pressure, $E_f = \rho_f e_f + 0.5\rho_f \vec{u}_f \cdot \vec{u}_f$ is the total energy of fluids. $\langle \bullet \rangle$ and $\tilde{\bullet}$ denote the phase-averaged and the mass-averaged variables, respectively. $\rho_{p,i}$ and $\vec{u}_{p,i}$ are the density and velocity of particle parcel *i*. $D_{p,i}$ is the drag force coefficient of parcel *i*. $\alpha_{p,i} = w_{i,f} V_{p,i} / V_f$ is the contribution of parcel *i* to the weighted particle volume fraction.

The particle phase is represented by discrete particle parcels consisting of multiple physical particles with same physical properties and kinetic properties[36]. The motion of particle parcel is governed by the Newton's second law (Eqs. 4 and 5).

$$\frac{d\vec{u}_p}{dt} = D_p\left(\vec{u}_f - \vec{u}_p\right) - \frac{1}{\rho_p}\nabla\left\langle p_f \right\rangle + \frac{1}{m_p}\sum_j \vec{F}_{C,j}\ , \tag{4}$$

$$\frac{d\vec{x}_p}{dt} = \vec{u}_p\ , \tag{5}$$

where $\vec{u}_i$ and $\vec{x}_i$ denote the velocity and displacement of parcel *i*, $\vec{F}_{C,j}$ represents the collision force between parcel *i* and *j*.

A four-way coupling strategy[37] was adopted to account for the momentum and energy transfer between gases and particles. Specifically the particle drag force and the associated work were incorporated into the momentum (Eq. 2) and the energy (Eq. 3) equations of the gas phase as the source terms, respectively. The particle parcels are driven by the pressure gradient force, drag force as well as the collision force between parcels (Eq. 4). Here the drag force coefficient was calculated using the De Felice model[38]. A soft sphere model represented by a coupling spring and dashpot was employed to model the collision force between parcels [36].

As to the algorithm solving the governing equations of gases, the weighted essentially nonoscillatory (WENO)[39] scheme was used to reconstruct the primary flow variables. A Riemann solver proposed by Harten Lax and van Leer (HLL)[40] was applied to obtain the intercell fluxes. The third-order Runge–Kutta method was applied for the time integration. The equations describing the parcel velocity and position were discretized by the Velocity-Verlet algorithm[41]. Bi-linear/tri-linear interpolation functions were adopted to calculate particle volume fraction and source terms in the Eulerian grids, as well as fluid quantities on Lagrangian parcels. Details

of the governing equations of CCFD-DPM and corresponding algorithms can be found in our previous studies[33, 42].

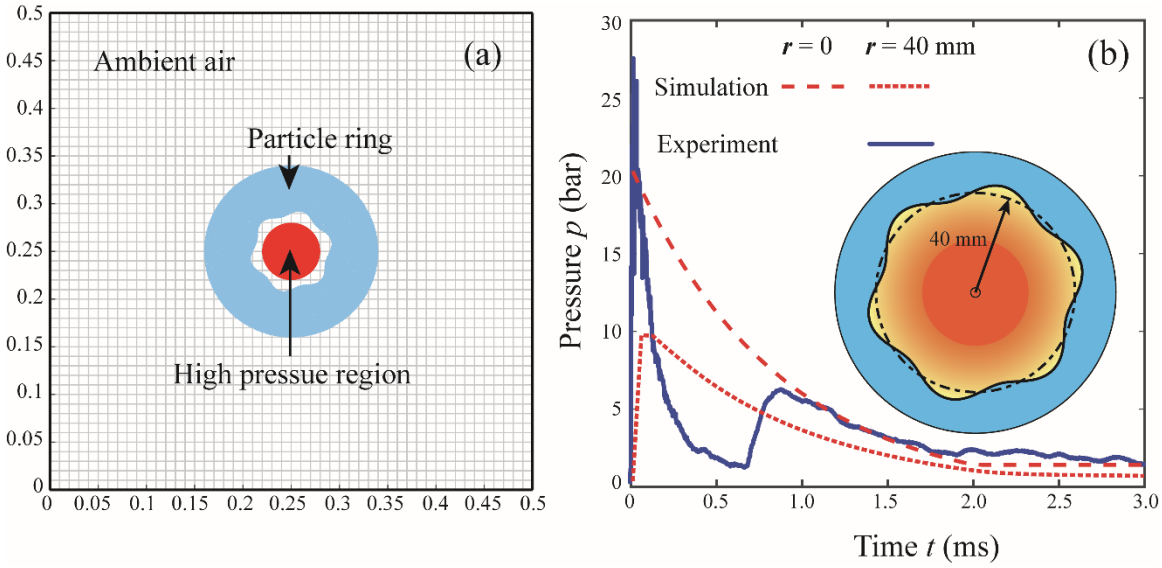

Figure 3 (a) Schematic of the numerical model. Note that the actual mesh width is one tenth of that shown in (a). (b) Pressure histories of the Eulerian gauges at the center (r = 0 mm) and the internal surface of ring (r = 40 mm) in simulations and the experiment in which $D_{in.0}$ = 80mm, $D_{out,0}$ = 180 mm, p_0 = 1 bar.

The two-dimensional numerical model presented in Fig. 3(a) has the particle ring with the geometry and the disturbed internal surface same as in the experiment where $D_{in,0}$ = 80 mm, $D_{out,0}$ = 180mm. The packing density and particle density were set to the values used in experiments. The particle diameter is set to be 100 μm. The whole parcel assemble consists of 63220 randomly arranged parcels whose diameters vary from 356 to 778 μm.

The shock loading was realized by setting a high pressure central area with the diameter matching that of the tube exit in experiments. The pressure profile inside

the central region was chosen in such way that the peak overpressure and the impulse at the internal surface of particle ring (r = 40mm) are comparable to those measured in the experiments. Specifically, the pressure inside the central region decays exponentially from 20 to 2 bar during the first two milliseconds. The overall pressure field was allowed to evolve on its own afterwards. The pressure profiles inside the central region (r =0) and at the internal surface of ring (r = 40 mm) compared with the experimentally registered pressure history at r = 40 mm are displayed in Fig. 3 (b). The impulses at r = 40 mm attained in simulation and experiment are 949.16 and 1108 Pa·s.

The restitution coefficient of parcels is 0.1 which takes into account of the energy dissipation inside the parcel; the normal stiffness of contacts between parcels is 2e7 N/s. In this work time step for CCFD module was determined by the CFL number which was set as 0.25 considering the numerical stability. In high Mach flow the characteristic time of flows is about several micro-second on the same order of that of particle-particle collisions. Thus time step for the DPM module was set as the same with the time step of CCFD module.

Results and Discussions

Fig. 4(a) and (b) display sequences of high-speed images showing the complete processes of the internal surface deformation alongside the global expansion of the particle ring in two typical cases, namely $D_{in,0}$ = 55 mm, $D_{out,0}$ = 180 mm, p_0 = 1.5 bar in Fig. 4(a) and $D_{in,0}$ = 80 mm, $D_{out,0}$ = 180 mm, p_0 = 1.0 bar in Fig. 4(b). As the

incident cylindrical shock encounters the internal interface, a compaction wave represented by the front of an annular compacted band trails far behind the transmitted wave with an average speed of 25-35 m/s (see the first frame in Fig.4(a)). Prior to the reflection of the rarefaction front on the external surface, the shocked internal surface largely retains its sinusoidal profile. Afterwards the growth of the perturbation amplitude begins to accelerate and the profile of the internal surface increasingly loses its symmetry. Eventually the internal surface evolves into an unsymmetrical structure with the ridge-like “fingers” thrusting inwards and petal-like wide “bubbles” protruding outwards. At the late stage (see last frame in Fig. 4(b)), small ripples stud the internal surface manifesting high-order harmonics. The morphological evolution of internal surfaces can be better discerned by superposing a sequence of profiles as shown in Fig. 4(d), in which the gap between two sequent profiles is colored according to the instantaneous velocity of internal surface. The gradual loosing of the sinusoidal symmetry is evident in Fig. 4(d). We fit the instantaneous profiles of internal surfaces with sinusoidal functions and attained the confidence coefficient χ which monotonically decreases with time. The plot of χ vs. time (*Appendix III*) shows a kink defining an onset of accelerating deviation from the symmetric sinusoidal shape. We refer the kink time t_χ to the stable-to-unstable transition of the instability pattern. Comparing the temporal variations of the internal

surface velocity and χ (*t*) we find the stable-to-unstable pattern transition corresponds to the end of the acceleration phase of internal surface (*Appendix III*)).

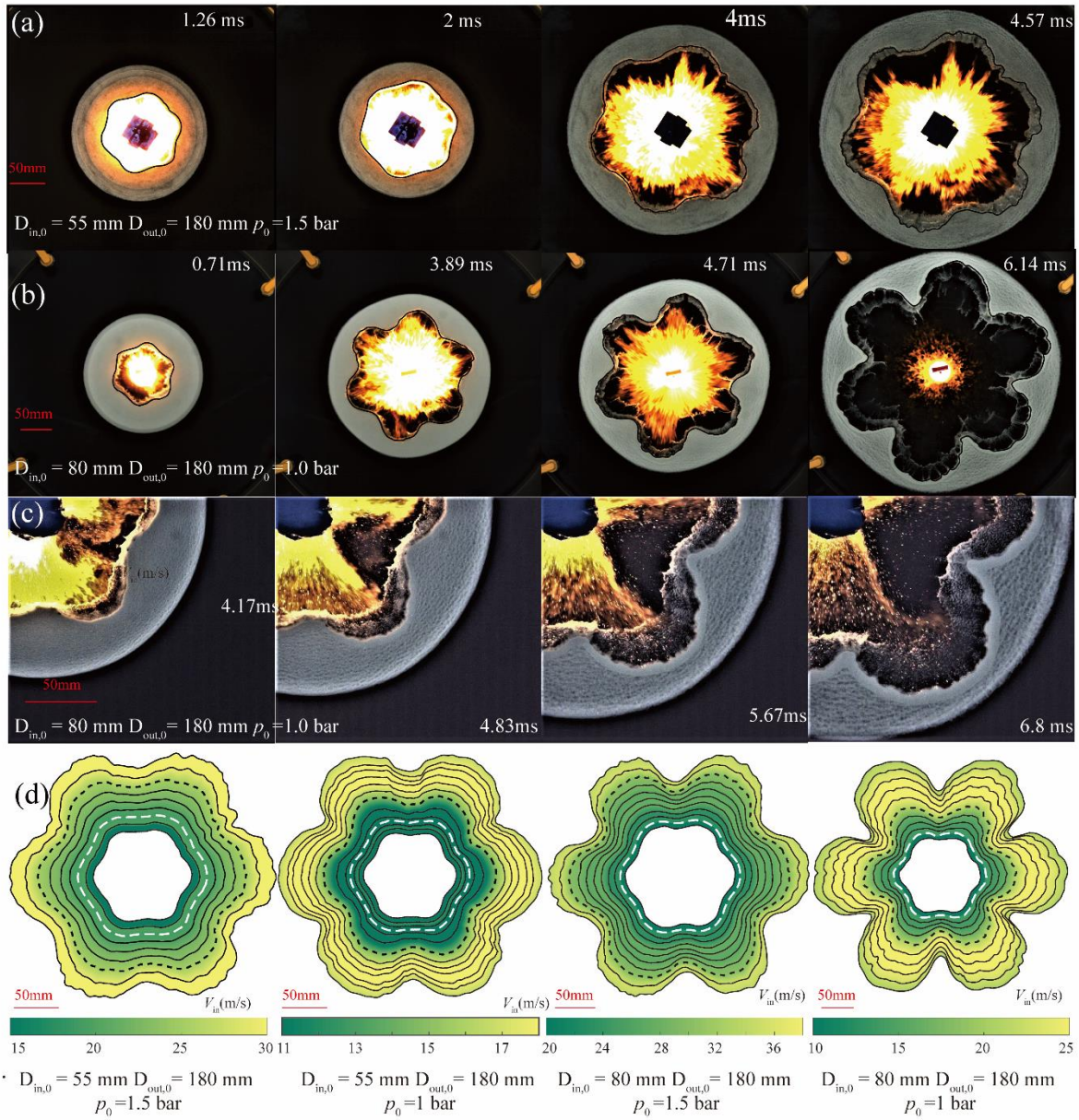

Figure 4. (a)(b) Temporal evolution of shock dispersed particles rings for two typical cases. (c) Closeup images of the shock dispersed particle ring before and after the stable-to-unstable pattern transition t_χ (*Appendix III*). The bulk of ring is permeated with a large number of voids while high-order harmonics are developing along the internal surface. (d) Superpositions of sequences of

internal surface profiles for four typical cases. From left to right, the times of the innermost internal surface profiles are 1.286, 1.571, 1.286 and 1.571 ms; the time intervals between two sequent profiles in each frame are 0.428, 0.428, 0.286 and 0.571ms. The gap between two sequent profiles is rendered in accordance with the instantaneous velocity. The profiles denoted by white dashed curves correspond to the rarefaction reflection from the external surface. The profiles denoted by black dotted curves correspond to the stable-to-unstable pattern transition t_χ.

Also evident from Fig. 4(d), when external boundaries expand to the same diameter, particle rings with the increased thickness and/or subjected to shocks with higher overpressures more likely remain the sinusoidal shaped internal surface, suggesting a retarded unstable regime. The closeup images in Fig. 4(c) show rich structural details inside the bulk of ring just prior to and after the stable-to-unstable pattern transition $t\chi$. After $t\chi$, the bulk of ring becomes textured, permeated by profuse tiny voids that first appear close to the external surface, then rapidly spread inward. The textured structure becomes coarser as the voids grow and coalesce with each other. Interestingly a compacted narrow strip along the internal surface remains intact throughout so as to prevent the erosion of the internal surface by the ever-growing voids.

Temporal variations of the perturbation amplitude a for all cases with varying $D_{\text{in},0}$, $D_{\text{out},0}$, and p_0 are plotted in Fig. 5(a). The inset of Fig. 5(a) shows a crossover between the exponential and linear growth of the perturbation amplitude in all cases while both the exponential coefficient and linear slope vary from case to case. However, the main panel in Fig. 5(a) shows that all the data can be scaled onto a single master curve which can be piecewisely fitted by a first exponential segment

before τ_c^* and a second linear segment after τ_c^*. The collapse is obtained by normalizing the time with the reflection time of the rarefaction front upon the external surface, t_{ref}, and the amplitude of perturbation by $\alpha = k\,(a - a_0)$, where k is the wavenumber. This way we can normalize out the overall pressure impulse effect since t_{ref} incorporates the effects of the overpressure of incident shock, the mass and thickness of ring, and the initial packing fraction as well. With the growth of perturbation amplitude transitioning from exponential to linear, the instability pattern progressively transitions from stable to unstable (*see Appendix III*), indicating a concurrence between the perturbation growth regime crossover and the pattern transition. Analogous to RM instability, here the "fingers" protruding inwards are referred to as spikes while the petal-like edges pushed outwards by the gases are referred to as bubbles. Fig. 5(b) shows the scaled amplitude histories for the spike and bubble, $\alpha_s = k(a_s - a_0/2)$ and $\alpha_b = k(a_b - a_0/2)$, where a_s and a_b refer to the amplitudes of the spike and bubble with respective to the reference undisturbed interface surface (see insets in Fig. 5(b)). Before τ_c^*, the symmetry of $\alpha_s(\tau)$ and $\alpha_b(\tau)$ suggests a symmetric stable pattern. Thereafter $\alpha_b(\tau)$ progressively lags behind the absolute value of $\alpha_s(\tau)$, breaking the symmetry of the internal surface. Clearly the growth law of the perturbation amplitude shown in Fig. 5(a) and (b) contradicts the conventional RM nonlinear theory appropriate for $\alpha > 1$ which forecasts asymptotic behaviors for α, α_s and α_b[43].

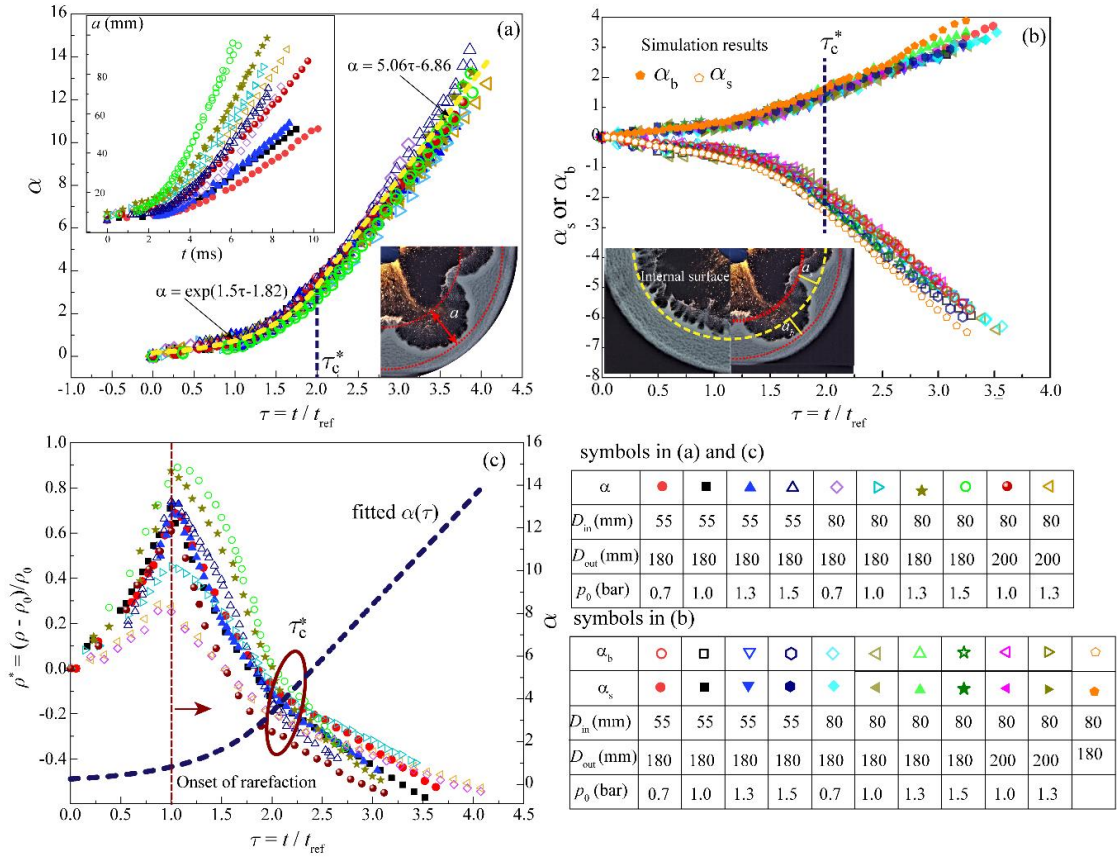

α										
D_{in} (mm)	55	55	55	55	80	80	80	80	80	80
D_{out} (mm)	180	180	180	180	180	180	180	180	200	200
p_0 (bar)	0.7	1.0	1.3	1.5	0.7	1.0	1.3	1.5	1.0	1.3

α_b											
α_s											
D_{in} (mm)	55	55	55	55	80	80	80	80	80	80	80
D_{out} (mm)	180	180	180	180	180	180	180	180	200	200	180
p_0 (bar)	0.7	1.0	1.3	1.5	0.7	1.0	1.3	1.5	1.0	1.3	

Figure 5. (a) Scaled master curve of the overall amplitude $\alpha = n/R_{in}\,(a - a_0)$ (a is defined in the inset below) verse time $\tau = t/t_{ref}$. Perturbation growth is characterized by an exponential regime ($\alpha = \exp(1.5\,\tau - 1.82)$) before τ_c^* and a linear regime ($\alpha = 5.06\,\tau - 6.86$) after τ_c^*. The fitted piecewise function is plotted by the yellow dashed curve. Inset: overall amplitude a versus time for experiments with different ring thickness and initial pressure of premixed gases. (b) scaled amplitudes of the bubble and spike, α_s and α_b, versus scaled time. Inset: snapshots of a reference particle ring with smooth internal surface (left) and a particle ring with perturbed internal surface (right). (c) Comparison between the temporal variations of scaled packing density and scaled overall amplitude fitted by the piecewise function.

The comparison between the temporal variations of the scaled perturbation amplitude and the scaled packing density $\rho^*=(\rho_p-\rho_{p,0})/\rho_{p,0}$ (see Fig. 5(c)) reveals an

explicit correlation between the bulk deformation of granular rings and the growth of interfacial perturbation amplitude. After peaking at $\tau = 1$, ρ^* undergoes first a rapid and then a relatively slow decline (see Fig. 5(c)). The onset of the decline of ρ^* ($\tau = 1$) coincides with the onset of the noticeable growth of a^*. The transition between rapid and slow decline of ρ^* remarkably coincides with t_c^*, the time demarcating the exponential and linear growth regimes of a^*. Hence the interfacial perturbation growth is closely associated with the bulk granular flows characterized by the dramatic changes of packing density caused by the compaction and the subsequent rarefaction waves. On the contrary, the compressible RM instability usually assume a constant uniform compression of shocked fluids only taking place during the early linear stage[43]. Therefore the granular RM-like instability invokes a mechanism fundamentally different from the RM instability.

The first rapid decrease of ρ^* is initiated by the inward traveling rarefaction fans when the compacted particles dilate into a random loose packing (RLP). Due to the lack of cohesion ρ^* would continue to decrease below the density of RLP, commencing an over-dilation. Lower than the threshold of RLP, the over-dilation cannot be sustained only by the re-arrangement of particles. Instead the emergence and growth of voids throughout the bulk as seen in Fig. 4(c) dominate the over-dilation, which is also found in our simulations (Fig.6). It is worth noting that the over-dilation is characterized by particle clustering rather than homogeneous dispersal of grains , which may well be attributed to the grain-scale heterogeneous compaction intrinsic to the granular media[21, 22]. Particle clusters percolated by strong force chains

experience exceedingly high compression during the shock compaction[5]. Accordingly, they remain intact for a longer time during the bulk dilation while particles in other areas loose contact with each other sooner. The growth and coalescence of voids decrease the global packing density not as effectively as the prior rarefaction waves as suggested by the slower decline rate of ρ^* after t_c^*.

The dynamics of particles subject to shock waves is closely associated with the pressure diffusion and the gas filtration which in turn are affected by the compression and dilation of the material skeleton. The CCFD-DPM simulations provide us insights on how the pressure gradient forces and drag forces evolve and meanwhile initiate the heterogeneous localized granular flows. The simulations successfully reproduce the growth of perturbation amplitude consistent with the experimental results as shown in Fig. 5(b). Fig. 6(a-e) present the fields of diffusion pressure, drag forces, particle velocities, circumferential particle velocities and packing densities during the shock dispersal. Once the incident divergent shock wave head on impinges the internal surface of particle ring, the shock focusing and reflection upon the convex edges (bubble edges) of the internal surface generate high pressure areas inside bubbles (Fig. 6(a-i)), invoking herein higher fluid velocity and resultant higher drag forces in the vicinity (Fig. 6(b-i)). Accordingly the isobaric lines and the envelop of the drag force field resemble an orthohexagnal shape whose symmetric axis are aligned with those of the sinusoidal internal surface (Fig. 6(a-ii) and (b-ii)). The particles in the vicinity of bubble edges thereby are driven by stronger pressure gradient forces and drag forces as well, and move faster than other areas (Fig. 6(c-

i)-(c-v)). Faster moving particle clusters tend to bifurcate transversely due to the weaker lateral collision forces, giving rise to the transverse granular flows from the bubble edges to the spike edges (Fig. 6(d-i)-(d-v)). Notably the packing density undergoes compression and ensuing dilation (Fig. 6 (e-i) to (e-v)) as observed in experiments. Specifically the over-dilation stage (Fig. 6 (e-iv) and (e-v)) in which the overall packing density is below that of RLP sees the permeating tiny voids as seen in experiments. As shown in Fig. 6(g) and (h) the hydrodynamic effects in terms of the pressure gradient forces and drag forces quickly attenuate and become negligible during the most part of the perturbation growth regime thanks to the short-lived shock loadings and the divergent configuration.

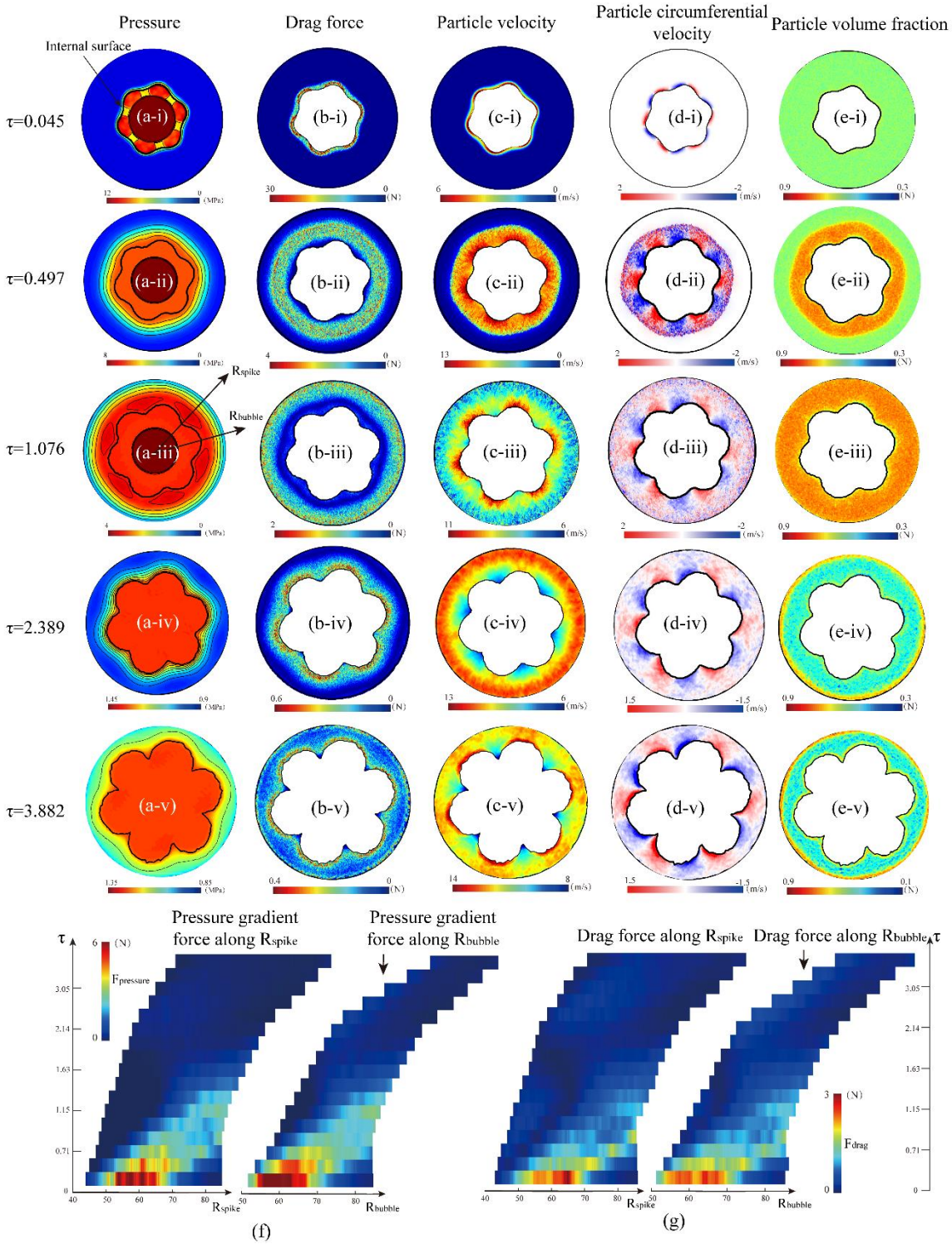
Pressure
Drag force
Particle velocity
Particle circumferential velocity
Particle volume fraction
Internal surface
τ=0.045
τ=0.497
τ=1.076
τ=2.389
τ=3.882
(a-i)
(b-i)
(c-i)
(d-i)
(e-i)
(a-ii)
(b-ii)
(c-ii)
(d-ii)
(e-ii)
(a-iii)
(b-iii)
(c-iii)
(d-iii)
(e-iii)
(a-iv)
(b-iv)
(c-iv)
(d-iv)
(e-iv)
(a-v)
(b-v)
(c-v)
(d-v)
(e-v)
Rspike
Rbubble
(MPa)
(N)
(m/s)
Pressure gradient force along Rspike
Pressure gradient force along Rbubble
Fpressure
Rspike
Rbubble
τ
(f)
Drag force along Rspike
Drag force along Rbubble
Fdrag
(g)

Figure 6. Numerical simulation generated fields of pressure (a-i)-(a-v), drag forces (b-i)-(b-v), particle velocity (c-i)-(c-v), particle circumferential velocity (d-i)-(d-v), and packing density (e-i)-(e-v) for the particle ring with $D_{in,0}$ = 80mm, $D_{out,0}$ = 180mm. (f) and (g) represent the pressure gradient forces $F_{pre} = \nabla p \cdot V_{parcel}$ (f), where V_{parcel} is the volume of parcel, and drag forces (g) along the symmetrical axis of bubble edge R_{buble} and spike edge R_{spike}, respectively. The symmetrical axis of bubble edge R_{buble} and spike edge $R_{spike.}$ are denoted in (a-iii).

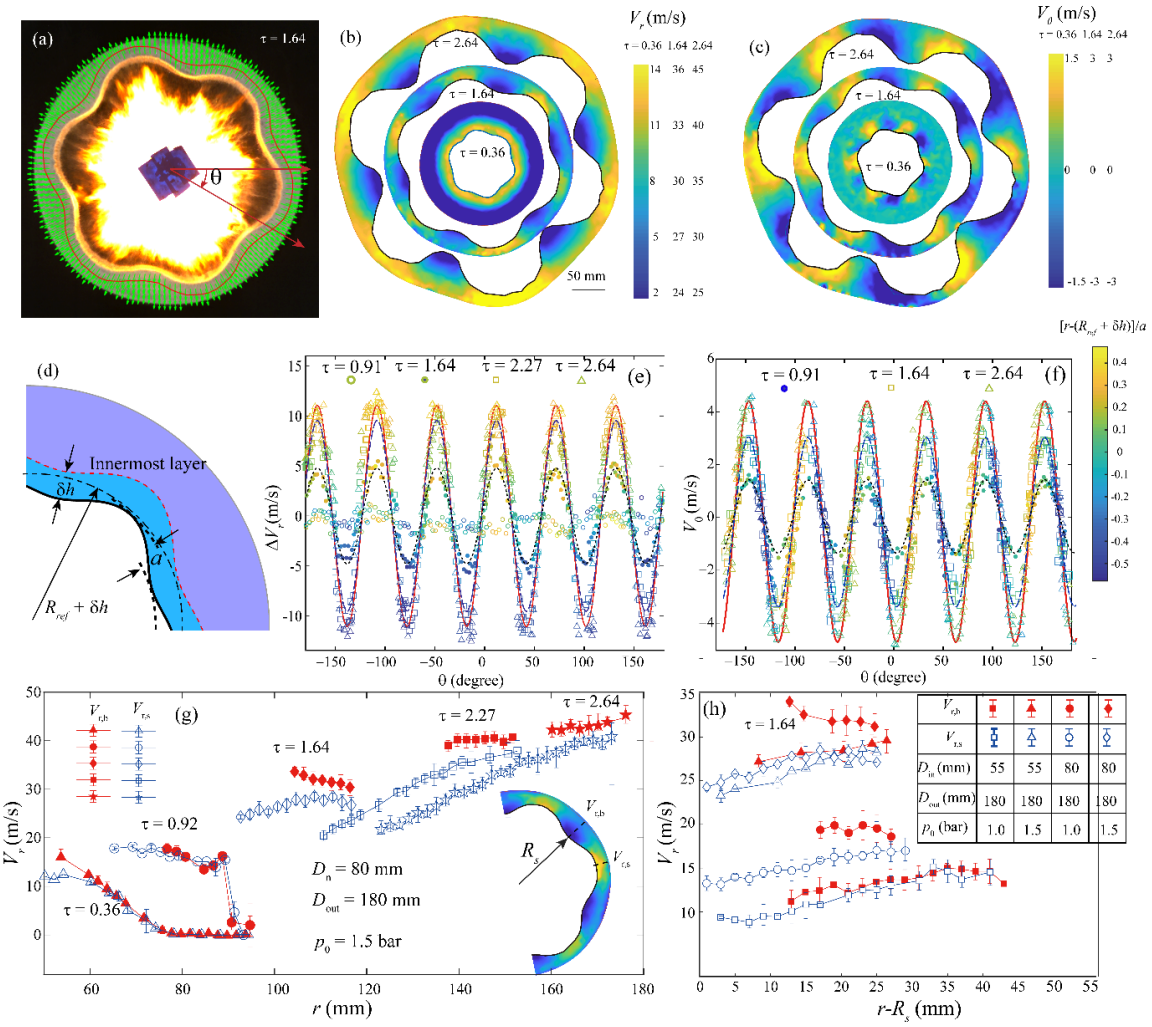

Figure 7. (a) Instantaneous PIV velocity field of the particle ring. (b) and (c) are superimpositions of a sequence of coarse grained PIV radial (b) and circumferential velocity fields (c). (d) Schematic of

the innermost layer with the thickness of δh = 8 mm the azimuthal variations of whose radial and circumferential velocities are plotted in (e) and (f). The shades of symbols in (e) and (f) which represent PIV grids inside the innermost layer (d) are in accordance with the scaled radial distance of PIV grid with respective to $R_{ref} + \delta h$, $[r - (R_{ref} + \delta h)]/a$, where R_{ref} is the radius of the reference unperturbed internal surface of particle ring. (g) Temporal variations in radial velocities along the symmetrical axis of the bubble edges and spike edges, $V_{r,b}$ and $V_{r,s}$. Note that the experiment data displayed in (a-c), (e-g) is from the case with $D_{in,0}$ = 80mm, $D_{out,0}$ = 180mm, p_0 = 1.5 bar. (h) Profiles of $V_{r,b}(r)$ and $V_{r,s}(r)$ for four typical cases at the same scaled time τ = 1.64.

The velocity fields attained by the PIV are presented in Fig. 7 (a-c) which retain the characteristics of velocity fields produced by simulations (Fig. 6(c-v) and (d-v)). Specifically the transvers flows from bubble edges to spike edges despite being weak are apparent from the very beginning of shock loading (Fig. 7(c)). To characterize the localized granular flows in the innermost layers as schematized in Fig. 7(d), we plot the azimuthal variations of radial and tangential velocities herein, $\Delta V_r(\theta) = V_r(\theta) - V_{r,in}$ and $V_\theta(\theta)$ (see Fig. 7(e) and (f)), where $V_{r,in}$ is the radial velocity of the reference internal surface. Regardless of times, $\Delta V_r(\theta)$ and $V_\theta(\theta)$ both exhibit a sinusoidal shape with one quarter of phase shift in between. The maxima and minima of $\Delta V_r(\theta)$ occur at the bubble cusps and spike apexes of internal surface, while the transverse flows are most pronounced at the midway between peaks and troughs of internal surface as happens in simulations. The amplitude of the sinusoidal shaped $\Delta V_r(\theta)$ is indicative of how fast the perturbation grows, while the transverse granular flows are responsible for the widening of bubbles and the narrowing of spikes shown in Fig. 4 and Fig. 6. The amplitudes of $\Delta V_r(\theta)$ shoots up

upon the onset of the rarefaction dilation (comparing τ = 0.91 and τ = 1.64 in Fig. 7(e)), signifying the acceleration of the perturbation growth. After the over-dilation sets in (τ = 2), little changes in the profiles of $\Delta V_r(\theta)$ and $V_\theta(\theta)$ can be detected (comparing τ = 2.27 and τ = 2.64 in Fig 7(e) and (f)), corresponding to the linear growth stage of the perturbation amplitude.

Fig. 7(g) shows the radial variations of V_r along the radii cutting through the peaks and troughs of the internal surface, namely $V_{r,b}(r)$ and $V_{r,s}(r)$ (see inset in Fig.7(g)). The distinct evolution of $V_{r,b}(r)$ and $V_{r,s}(r)$ shed more light on the differences of localized granular flows beyond the bubble and spike edges of internal surface. The $V_{r,b}(r)$ and $V_{r,s}(r)$ both display an exponential decay in the wake of the compaction wave and a plateau after the compaction wave almost compasses all particles, no significant differences between them discernable. Immediate after the onset of the rarefaction dilation (τ = 1), the $V_{r,b}(r)$ jumps above the $V_{r,s}(r)$ while both are gradually elevated throughout the dilation stage. Contrasting with the linear positive gradient of $V_{r,s}(r)$ towards the external boundary, the profiles of $V_{r,b}(r)$ features a plateau or even negative slope. Similar radial profiles of $V_{r,s}(r)$ and $V_{r,b}(r)$ can be found in the simulated dilating ring (Fig.6 (c-v)). The characteristics of the profiles of $V_{r,b}(r)$ and $V_{r,s}(r)$ evident in Fig. 7(g) are universal cross all the cases studied here as shown in Fig. 7(h).

Since neither the diffusion pressure nor drag forces have substantial effects for the most part of the dilation phase, the evolution of $V_{r,s}(r)$ and $V_{r,b}(r)$ predominately result

from the rarefaction effects on the dry particles without cohesion. As illustrated in the left inset of Fig. 8, in the wake of the inward traveling rarefaction wave, the elastic energies stored inside the contact points between particles would be transmitted outward from pair to pair and transformed to kinetic energies of particles all the way down to the outmost layers. Thereby closer to the external boundary the particles, faster they move outwards. The rarefaction dilation effect leads to a positive gradient of $V_r(r)$ towards the external surface. The energy transmission and transformation proceed until the particles begin to loose contact with each other which commences from the external boundary. At the end of the dilation, all elastic energies are transformed to the kinetic energies of particles so that the profiles of $V_{r,s}(r)$ and $V_{r,b}(r)$ remain consistent thereafter.

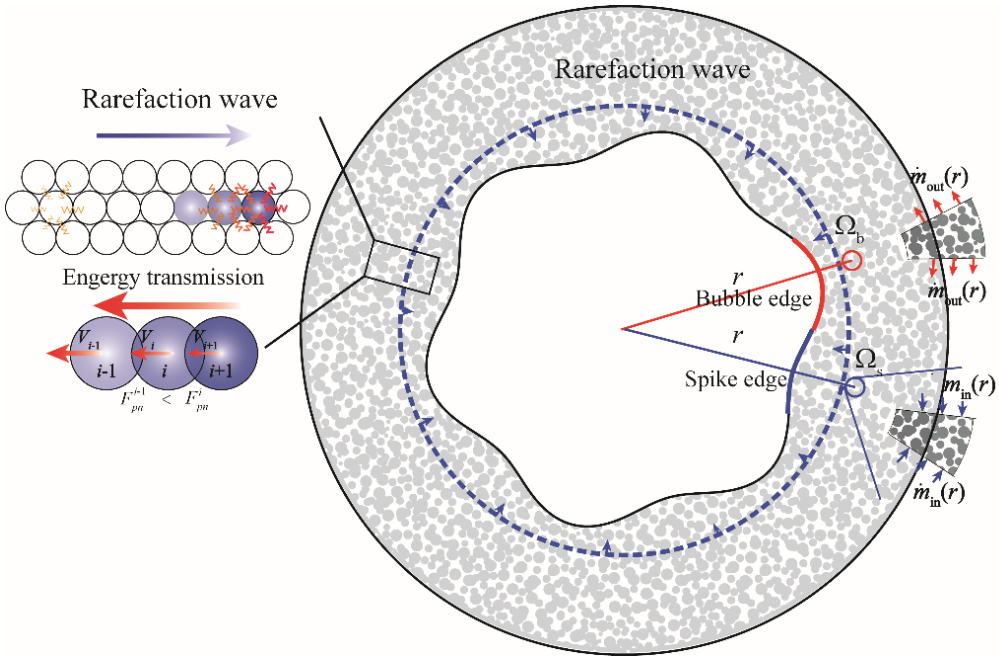

Figure 8. Schematic of the rarefaction effect (left inset), the flow-out and flow-in mass effects (right inset) during the rarefaction dilation stage of particle ring. Left inset: Inward traveling rarefaction

wave releases the elastic energy stored in the contact points of particle pairs. Particle pairs closer to the internal surface store larger elastic energy. Alongside the propagation of the rarefaction wave, the energy is transmitted outwards through the contact points and meanwhile transferred into the kinetic energy. Particles further away from the internal surface gain more energy and move faster. Right inset: two representative control volumes aligned with the symmetrical axis of the bubble edge and spike edge, Ω_b and Ω_s. Ω_b and Ω_s have the same radii. Ω_b squeezes out particles transversely at a flow rate of $\dot{m}_{out}(r)$ while Ω_s entrains particles from lateral edges at a flow rate of $\dot{m}_{in}(r)$. $\dot{m}_{out}(r)$ and $\dot{m}_{in}(r)$ attenuate with the increasing *r*.

But why the particles beyond the bubble edges move faster than those beyond the spike edges as shown in Fig. 5(e)? The following simple analysis can illustrate how the transverse granular flows from bubbles to spikes conduce to the distinct profiles of $V_{r,b}(r)$ and $V_{r,s}(r)$. As schematized in the right inset of Fig. 6, the control volumes with the same radius but aligned with the central axis of bubble and spike edges, Ω_b and Ω_s, experience a net mass flow out and flow in, respectively. Thus the dynamics inside the Ω_b and Ω_s are described by force balance:

$$\left[m_b(r) - \dot{m}_{out}(r)\cdot\Delta t\right]\dot{V}_b(r) = \dot{m}_{out}(r)V_b(r) + F_{ext,b} \tag{6}$$

$$\left[m_s(r) + \dot{m}_{in}(r)\cdot\Delta t\right]\dot{V}_s(r) = -\dot{m}_{in}(r)V_s(r) + F_{ext,s} \tag{7}$$

where $m_b(r)$ and $m_s(r)$ are the mass in Ω_b and Ω_s with the velocities of $V_b(r)$ and $V_s(r)$, $\dot{m}_{out}(r)$ and $\dot{m}_{in}(r)$ are the net mass flow rates out of Ω_b and into Ω_s, $F_{ext,b}$ and $F_{ext,s}$ represent the external forces exerting on the Ω_b and Ω_s. The external forces mainly consist of the pressure gradient forces, F_{pre}, the drag forces, F_{drag}, and the net

particle collision forces, F_{col}. F_{pre} and F_{drag} are only relevant during the very early times of dilation (see Fig. 6(g) and (h)). Since F_{col} mainly depends on the velocities of compacted particles and particle friction (*Appendix IV*), we have $F_{col,s} \approx F_{col,b}$. According to Eqs. (1) and (2), Ω_b with diminishing mass gains larger acceleration than Ω_s with added mass, namely $\dot{V}_s(r) < \dot{V}_b(r)$. As a result, particles ahead of bubble edges move faster than those ahead of spike edges. The transverse flows attenuate towards the external surface so that the flow-out and flow-in mass effect decays alongside. For particles pushed by spike edges, the flow-in mass effect augments the rarefaction dilation effect, particles closer to the internal surface further slowing down. On the contrary, the flow-out mass effect offsets the rarefaction dilation effect for particles pushed by bubble edges, leading to a plateau or even slightly slope down shape of $V_{r,b}(r)$ as seen in Fig. 7(g).

The opposite radial variations in $V_{r,s}(r)$ and $V_{r,b}(r)$ suggest stronger dilation beyond the spike edges than that beyond the bubble edges. Particles ahead of bubble edges tend to migrate into adjacent spike areas where voids are more abundant, sustaining the transverse particle flows. Therefore the distinct profiles of $V_{r,s}(r)$ and $V_{r,b}(r)$ and the transverse particle flows are strongly interdependent and feed into each other. Larger the difference between $V_{r,s}(r)$ and $V_{r,b}(r)$, stronger the transverse particle flows and *vice versa*. This self-feedback propels the growth of perturbation and the pattern evolution as well. The smaller difference between $V_{r,s}(r)$ and $V_{r,b}(r)$ for thicker particle rings (D_{in} = 55 mm, D_{out} = 180 mm, see Fig. 7(h)) implies small growth rate and slower pattern changes. The first and foremost element in the mechanism

is the hydrodynamic initiation of the incipient transverse particle flows which is amplified by the rarefaction dilation.

Conclusion

In contrast with the linear growth followed by the nonlinear asymptotic growth of perturbation amplitude in RM instability, the granular RM-like instability displays an exponential growth regime followed by a linear growth regime. The drastic difference of perturbation growth law arises from the fundamentally different physics. RM instability originates from the induction of baroclinic vorticity along the interface while the granular RM-like instability heavily involves the bulk deformation which dramatically changes during the shock compaction, the rarefaction dilation and the inertial over-dilation stages. During the shock compaction, the global deformation is overwhelmingly characterized by uniform divergent flows when the perturbation amplitude barely grows. Whereas the hydrodynamic effects at the very early instants introduce weak but critical transverse granular flows from bubble edges to spike edges which are significantly amplified upon the rarefaction dilation. It is the transverse granular flows that conduce to the emergence of heterogeneous flows. Specifically, particles beyond the bubble edges increasingly move faster than those beyond the spike edges, resulting in the exponential growth of perturbation amplitude. Meanwhile the azimuthal variations in radial velocity in turn sustain and reinforce the transverse granular flows so as to break the symmetry of the sinusoidal shape of internal surface. The coupling between the heterogeneous radial flows and transverse flows cannot survive during the over-dilation stage when the granular

medium disintegrates into a large number of particle clusters. From then on both radial and transverse velocity fields remain unvaried, bringing about the linear growth of perturbation amplitude.

Acknowledgments

This work was supported by the National Natural Science Foundation of China (nos. U1730111, 11972088, 11732003) and the State Key Laboratory of Explosive Science and Technology (no. QNKT19-05).

References

1. Y. Formenti, T. H. Druitt,K. Kelfoun Characterisation of the 1997 Vulcanian explosions of Soufrière Hills Volcano, Montserrat, by video analysis. *Bulletin of Volcanology* 65(8):587-605(2003).

2. V. Rodriguez, R. Saurel, G. Jourdan and L. Houas, Phys. Rev. E **88** (6), 063011 (2013).

3. K. Kandan, S. N. Khaderi, H. N. G. Wadley and V. S. Deshpande, Journal of the Mechanics and Physics of Solids **109**, 217-240 (2017).

4. K. Xue, K. Du, X. Shi, Y. Gan and C. Bai, Soft Matter (2018).

5. K. Xue, P. Han, K. Du, Y. Gan, Z. Wang and C. Bai, Soft Matter **16** (6), 1498-1517 (2020).

6. R. D. Richtmyer, **13** (2), 297-319 (1960).

7. E. E. Meshkov, Fluid Dynamics **4** (5), 101-104 (1969).

8. Y. Zhou, Physics Reports **720-722**, 1-136 (2017).

9. X. Luo, M. Li, J. Ding, Z. Zhai and T. Si, Journal of Fluid Mechanics **877**, 130-141 (2019).

10. Y. Forterre and O. Pouliquen, Ann.Rev.Fluid Mech **40**, 1-24 (2008).

11. C. Ancey, J. Non-newton. Fluid **142** (1-3), 4-35 (2007).

12. J. I. N. Sun and S. Sundaresan, Journal of Fluid Mechanics **682**, 590-616 (2011).

13. S. Chialvo, J. Sun and S. Sundaresan, Physical Review E - Statistical, Nonlinear and Soft Matter Physics **85** (2) (2012).

14. S. Sundaresan, A. Ozel and J. Kolehmainen, Annual Review of Chemical and Biomolecular Engineering **9** (1), 61-81 (2018).

15. B. Sandnes, H. A. Knudsen, K. J. Måløy and E. G. Flekkøy, Physical Review Letters **99** (3), 038001 (2007).

16. X. Cheng, L. Xu, A. Patterson, H. M. Jaeger and S. R. Nagel, Nature Physics **4**, 234 (2008).

17. H. Huang, F. Zhang, P. Callahan and J. Ayoub, Physical Review Letters **108** (25), 258001 (2012).

18. J. L. Vinningland, Ø. Johnsen, E. G. Flekkøy, R. Toussaint and K. J. Måløy, Physical Review Letters **99** (4), 048001 (2007).

19. C. P. McLaren, T. M. Kovar, A. Penn, C. R. Müller and C. M. Boyce, PNAS **116** (19), 9263-9268 (2019).

20. A. H. Clark, L. Kondic and B. R. P., Physical Review Letters **109**, 238302 (2012).

21. J. Y. Huang, L. Lu, D. Fan, T. Sun, K. Fezzaa, S. L. Xu, M. H. Zhu and S. N. Luo, Scripta Materialia **111**, 114-118 (2016).

22. R. S. Crum, M. A. Homel, D. C. Pagan, E. B. Herbold, D. Miller, J. Lind, B. J. Jensen, A. J. Iverson and M. C. Akin, J. App. Phys. **125** (2), 025902 (2019).

23. A. Britan and G. Ben-Dor, International Journal of Multiphase Flow **32** (5), 623-642 (2006).

24. G. Ben-Dor, A. Britan, T. Elperin, O. Igra and J. P. Jiang, Experiments in Fluids **22** (5), 432-443 (1997).

25. F. Zhang, D. L. Frost, P. A. Thibault and S. B. Murray, Shock Waves **10** (6), 431-443 (2001).

26. A. Milne, C. Parrish and I. Worland, Shock Waves **20** (1), 41-51 (2010).

27. K. Xue, Q. Yu and C. Bai, Eur. Phys. J. E. **37** (9), 88 (2014).

28. Kun Xue, Jiaqi Liu, Chun Feng, Yixiang Gan and C. Bai, Chemical Engineering Science **202**, 250-269 (2019).

29. R. Epstein, **11** (11), 5114-5124 (2004).

30. R. M. Lueptow, A. Akonur and T. Shinbrot, Experiments in Fluids **28** (2), 183-186 (2000).

31. D. Gollin, W. Brevis, E. T. Bowman and P. Shepley, Granular Matter **19** (3), 42 (2017).

32. M. Girardi, S. Radl and S. Sundaresan, Chemical Engineering Science **144**, 224-238 (2016).

33. BaoqingMeng, JunshengZeng, BaolinTian, LiLi, ZhiweiHe and XiaohuGuo, Phys. Fluids **31** (7), 074102 (2019).

34. W. Thielicke and E. J. Stamhuis, Journal of Open Research Software **2** (1), 355-364 (2014).

35. M. R. Baer and J. W. Nunziato, International Journal of Multiphase Flow **12** (6), 861-889 (1986).

36. S. Apte, K. Mahesh and T. Lundgren, Center for Turbulence Research Annual Research Briefs, 161-171 (2003).

37. S. Ukai, K. Balakrishnan and S. Menon, Phys. Fluids **22** (10), 104103 (2010).

38. R. Felice, Int.~J.~Multiphase Flow **20**, 153-159 (1994).

39. X. D. Liu, Journal of Computational Physics **115** (1), 200-212 (1994).

40. E. F. Toro, *Riemann solvers and numerical methods for fluid dynamics: A practical introduction*. (Springer Science & Business Media, 2013).

41. H. Kruggel-Emden, M. Sturm, S. Wirtz and V. Scherer, Computers and Chemical Engineering **32** (10), 2263-2279 (2008).

42. BaoqingMeng, JunshengZeng, BaolinTian, RuiZhou and WeidongShen, **9** (12), 125311 (2019).

43. W. H. Liu, C. P. Yu, W. H. Ye, L. F. Wang and X. T. He, Phys. Plasmas **21** (6), 062119 (2014).